

# Chromatin condensation fluctuations rather than steady-state predict chromatin accessibility

Nicolas Audugé, Sergi Padilla-Parra<sup>ID</sup>, Marc Tramier<sup>ID</sup>, Nicolas Borghi<sup>ID</sup>\* and Maité Coppey-Moisan<sup>ID</sup>\*

Institut Jacques Monod UMR 7592, Université de Paris - Centre National de la Recherche Scientifique, Paris, France

Received January 18, 2019; Revised April 24, 2019; Editorial Decision April 29, 2019; Accepted May 07, 2019

## ABSTRACT

**Chromatin accessibility to protein factors is critical for genome activities. However, the dynamic properties of chromatin higher-order structures that regulate its accessibility are poorly understood. Here, we took advantage of the microenvironment sensitivity of the fluorescence lifetime of EGFP-H4 histone incorporated in chromatin to map in the nucleus of live cells the dynamics of chromatin condensation and its direct interaction with a tail acetylation recognition domain (the double bromodomain module of human TAF<sub>II</sub>250, dBD). We reveal chromatin condensation fluctuations supported by mechanisms fundamentally distinct from that of condensation. Fluctuations are spontaneous, yet their amplitudes are affected by their sub-nuclear localization and by distinct and competing mechanisms dependent on histone acetylation, ATP and both. Moreover, we show that accessibility of acetylated histone H4 to dBD is not restricted by chromatin condensation nor predicted by acetylation, rather, it is predicted by chromatin condensation fluctuations.**

## INTRODUCTION

The regulation of multi-level chromatin compaction required for transcriptional activity in eukaryotic cells involves post-translational modifications of histones and their specific interactants, as well as histone chaperones and ATP-dependent chromatin remodelers. Histone acetylation was the first type of such modifications to be associated with gene transcription (1). Acetylation of histone, likely through the neutralization of positive charges, decreases its affinity to DNA (2), alters nucleosome conformation (3), pro-

motes the association of transcription factors with nucleosomes (4), and causes decondensation of chromatin higher-order structures (5,6), thereby providing possible mechanisms contributing to transcriptional activity. New probes now allow real-time imaging of histone acetylation (7). Yet, histone acetylation may only predict the potential for gene transcription, rather than transcription itself. Moreover, histone acetylation was also shown to increase its affinity to DNA (8), which further undermines its predictive power for transcription.

Hypersensitivity to nucleases has been the historical proxy to assess nucleosome organization and chromatin accessibility (9). The strength of this, and more recently derived approaches (accessibility to transposase, methyltransferase, isolation of crosslinked nucleosomes) is the ability to identify accessible sequences by sequencing of nucleosome-free fragments, which can reach single-cell to subnuclear resolution (10–12). However, these approaches do not inform on chromatin dynamics in live cells. In contrast, advances in fluorescence microscopy techniques have allowed the probing the intranuclear milieu permeability to presumably inert fluorescent particles and the mobility of chromatin interactants (13–17), chromatin motions (18–22), or chromatin-bound DNA torsional dynamics (23). These studies have revealed the existence of multi-scale chromatin dynamics, but their relationship to chromatin acetylation and accessibility remain poorly understood.

Here, we sought to directly assess the relationship between chromatin dynamics and accessibility, and its dependence on histone acetylation and ATP-dependent mechanisms. To do so, we leveraged the sensitivity of a fluorophore fluorescence lifetime to the local environment in live cells, which was previously shown to report chromatin condensation states in fixed cells (18). We combined this with direct assessment by FRET (Förster resonance energy transfer) of the interaction between acetylated H4 histone and

\*To whom correspondence should be addressed. Tel: +33157278041; Email: nicolas.borghi@ijm.fr

Correspondence may also be addressed to Maité Coppey-Moisan. Email: maite.coppey@ijm.fr

Present addresses:

Sergi Padilla-Parra, Wellcome Centre for Human Genetics, Cellular Imaging, University of Oxford, Oxford, UK; Division of Structural Biology, Wellcome Centre for Human Genetics, University of Oxford, UK; Dynamic Structural Virology Group, Biocruces Health Research Institute, Barakaldo, Spain; IKERBASQUE, Basque Foundation for Science, Bilbao, Spain.

Marc Tramier, Institut de génétique et développement de Rennes UMR 6290, BIOSIT – UMS 3480, Université de Rennes, Centre National de la Recherche Scientifique, Rennes, France.

human TAF<sub>II</sub>250 double bromodomain (24,25), a module conserved in histone acetyltransferases, bromodomain and extra-terminal domain protein families of transcriptional regulators, and ATP-dependent chromatin remodeling factors (26,27).

A detailed spatiotemporal analysis under hyper-acetylation, ATP depletion, and the combination of both conditions revealed spontaneous chromatin condensation fluctuations that are affected by distinct and competing mechanisms dependent on acetylation, ATP and both, and by their sub-nuclear localization. Moreover, the amplitude of these fluctuations predicts chromatin accessibility, which is not restricted by chromatin condensation.

## MATERIALS AND METHODS

### Plasmid constructs

Fluorescent fusion proteins were cloned in pEGFP-C1 (Clontech, Mountain View, CA, USA) and pmCherry-C1. To generate pmCherry-C1, the mCherry coding sequence was transferred from pRSETB-Cherry (a generous gift from Dr. Tsien, University of California at San Diego) into a Clontech vector backbone. H4 cDNA (IMAGE: 2130477, ResGen) was cloned in pEGFP-C1 vector using XhoI and SalI sites. The dBD sequence (containing the amino acids 1207–1872 of TAF<sub>II</sub>250) was obtained from Kanno *et al.* (24) and cloned in the pmCherry-C1 or in the pEGFP-C1 vector using EcoRI and KpnI sites.

### Cell culture and treatments

HEK 293 cells were cultured in Dulbecco's modified Eagle's medium containing 10% fetal bovine serum (PAA Laboratories GmbH, Pasching, Austria). The cultures were incubated at 37°C in a humidified atmosphere of 5% CO<sub>2</sub>. HEK293 cells were seeded on 32-mm round glass coverslip at a density of  $2 \times 10^5$  cells. At ~70% of confluence, cells were transfected with a total amount of 1 µg of expression vectors using Nanofectin I (PAA Laboratories, Inc). Twenty-four hours later, coverslips were mounted in an open observation chamber with DMEM-F12 without Phenol red, B12 vitamin and Riboflavin, and supplemented with 20 mM HEPES and L-glutamine (PAA). The histone deacetylase inhibitor sodium butyrate (NaB), sodium azide (Az), and deoxy-glucose (DG) were obtained from Sigma Aldrich (Stenheim, Germany). For NaB treatment, cells were incubated 24 h after transfection with 2.5 mM of NaB for 24 h before imaging. For ATP depletion, cells were incubated with 10 mM Az and 10 mM DG for 2 h before imaging. Histone acetylation was verified after acid-urea-Triton polyacrylamide gel electrophoresis (15% acrylamide, 0.1% *M*-bisacrylamide, 6 M urea, 5% acetic acid, 8 mM Triton X-100, 0.5% TEMED, 0.00025% riboflavin) by western blot with an anti-H4 primary antibody (07-108, Upstate, France), and peroxidase-conjugated secondary antibody (Amersham ECL western blotting kit) (Supplementary Figure S1A).

### Fluorescence lifetime acquisition

Cells were imaged on a two-photon FLIM system (TriM-FLIM) that combines multifocal multiphoton excitation

(TriMscope) and a fast-gated CCD camera (PicoStar), all controlled by the IMspector software (LaVisionBiotec, Bielefeld, Germany), as described elsewhere (25). Briefly, two-photon multifocal excitation is carried out using the TriMscope connected to an inverted microscope (IX 71, Olympus, Tokyo, Japan). A mode-locked Ti:Sa laser tuned at 950 nm for the excitation of enhanced green fluorescent protein (EGFP) (MaiTai Spectra Physics, Evry, France) is split into 64 beams with a 50/50 beam splitter and mirrors. The beams pass through a 2000 Hz scanner before illuminating the back aperture of an infrared water immersion objective (60×/NA 1.2, Olympus, Tokyo, Japan). A line of foci at the focal plane is scanned across the sample, generating a pseudo wide-field illumination. A wheel of spectral filters (520DF40, Chroma Technology, for EGFP) is used to select the fluorescence imaged onto a fast-gated light intensifier connected to a CCD camera (PicoStar). The gate of the intensifier is set to 2 ns. The intensifier acts as a very fast shutter for each delay from 0 to 10 ns along the fluorescence decay. 5 gates are necessary and sufficient to calculate the mean, instantaneous fluorescence lifetime ( $\tau$ ) of EGFP (25), by applying:  $\tau = \sum \Delta t_i \cdot I_i / \sum I_i$ , where  $\Delta t_i$  corresponds to the time delay after the laser pulse of the *i*th gated image acquired and  $I_i$  to the pixel intensity map in the *i*th gated image. The acquisition time of the CCD camera was set to 3 s, which determines the time resolution of a  $\tau$  image. The time-average of  $\tau$  ( $\bar{\tau}$  in the main text) and its temporal standard deviation ( $\sigma_\tau$ ) were calculated from 100 consecutive images for each pixel using ImageJ (W.S. Rasband, ImageJ, U.S. National Institutes of Health, Bethesda, MD, USA, <http://rsb.info.nih.gov/ij/>) (Supplementary Figure S1B). The steady-state fluorescence intensity shown in Figure 1 is the sum of the five gated images intensities ( $\sum I_i$ ) averaged over four consecutive images. The measured point spread function gives a *x*-*y* spatial resolution of 515 nm.

### Fluorescence lifetime analysis

**Data management and analysis.** Nuclear pixels were selected based on EGFP-H4 steady-state fluorescence intensity thresholding. Nuclear pixel coordinates were used to calculate the smallest distance of each nuclear pixel to the nucleus border ( $d$ ), the mean distance per nucleus of a nuclear pixel to the border ( $\bar{d}$ ) and its standard deviation ( $\sigma_d$ ), to retrieve the deviation of each nuclear pixel from the mean distance to the border ( $\delta = (d - \bar{d})/\sigma_d$ ), which typically ranged from -1.5 (close to the border) to 3 (far from the border). Peripheral pixels were defined as  $\delta \leq -1$  (~1 µm-wide) and central pixels as  $\delta \geq +1$  (Supplementary Figure S1C). Fluorescence lifetime data ( $\tau$ ,  $\bar{\tau}$ ,  $\sigma_\tau$ ) of every nuclear pixel in 7–15 cells were collected from at least 3 independent experiments for each condition and their distributions displayed in 'violin' plots, histograms, or 2D-plots depending on figures. All of the above was performed in MATLAB (MathWorks).

**Spatial correlation analysis.** The instantaneous fluorescence lifetime fluctuation spatial autocorrelation function of the FLIM image recorded at time *t* in a time series is given

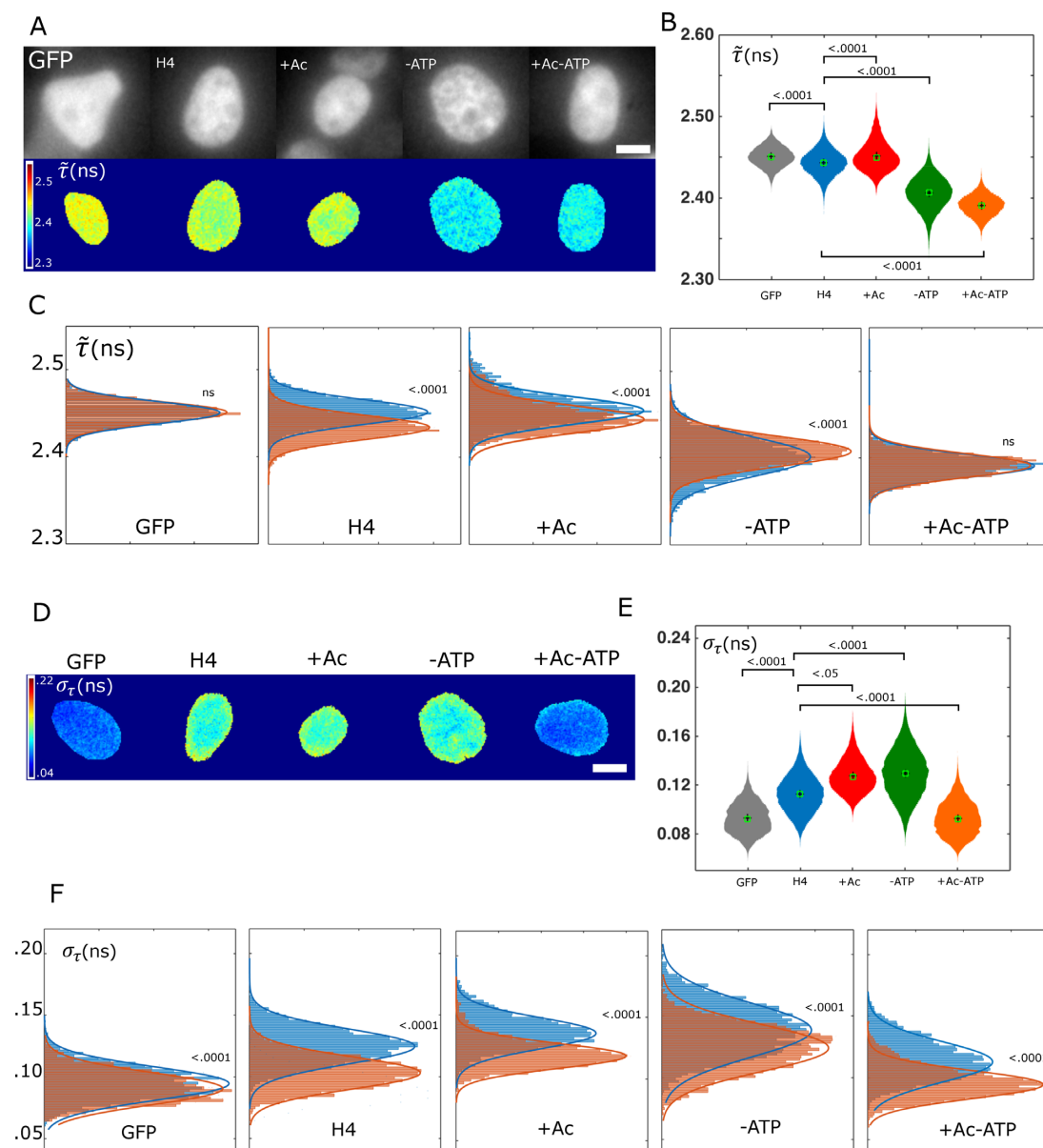


**Figure 1.** Chromatin condensation and its fluctuations depend on subnuclear localization, histone acetylation and metabolic state (A) Typical images of HEK cells expressing either free EGFP or EGFP-H4 in untreated (H4), hyper-acetylation (+Ac), ATP-depletion (−ATP), or both (+Ac-ATP) conditions. Top: steady-state fluorescence intensity, bottom: time-averaged fluorescence lifetime  $\tilde{\tau}$ . Bar = 5  $\mu\text{m}$ . (B) Time-averaged fluorescence lifetime  $\tilde{\tau}$  distributions in conditions above: EGFP (12 694 pixels, seven cells); EGFP-H4 (29 288 pixels, 15 cells); +Ac (17 405 pixels, nine cells); −ATP (32 425 pixels, 13 cells); +Ac-ATP (20 795 pixels, eight cells). Black cross: mean, green box: median. Kruskal–Wallis test. (C) Time-averaged fluorescence lifetime  $\tilde{\tau}$  distributions in conditions above for peripheral (blue) and central (orange) pixels and their Gaussian fits. Extra sum-of-squares  $F$  test with same fit for both distributions as null hypothesis. ns = not significant. (D) Typical images of fluorescence lifetime standard deviation  $\sigma_{\tau}$  in HEK cells expressing either free EGFP or EGFP-H4 in untreated (H4), hyper-acetylation (+Ac), ATP-depletion (−ATP), or both (+Ac-ATP) conditions. Bar = 5  $\mu\text{m}$ . (E) Distributions of fluorescence lifetime standard deviation  $\sigma_{\tau}$  in conditions above, same pixel and cell numbers as in Figure 1. Black cross: mean, green box: median. Kruskal–Wallis test. (F) Distributions of fluorescence lifetime standard deviation  $\sigma_{\tau}$  in conditions above for peripheral (blue) and central (orange) pixels and their Gaussian fits. Extra sum-of-squares  $F$  test.

by:

$$r(\varepsilon, \eta)_t = \frac{\langle \delta\tau(x, y) \delta\tau(x + \varepsilon, y + \eta) \rangle}{\langle \tau(x, y) \rangle_t^2}$$

where the angular brackets denote spatial averaging over the image,  $\varepsilon$  and  $\eta$  are spatial lag variables corresponding to

pixel shifts of the image relative to itself in the  $x$  and  $y$  directions and  $\delta\tau$  the difference between  $\tau$  and its spatial mean at  $t$ . Images are analysed by a MATLAB routine (a generous gift from David L. Kolin and Paul W. Wiseman) and the correlation functions calculated using Fourier methods and then fit to a 2D Gaussian, which half width at half maximum is the correlation length  $l$ .



**FRET quantification.** The mean transfer rate is defined by  $k_{\text{FRET}} = 1/\tau_{\text{D}} + 1/\tau_{\text{DA}}$ , in which  $\tau_{\text{D}}$  and  $\tau_{\text{DA}}$  are the donor fluorescence lifetime in the absence and in the presence of acceptor, respectively (28). For each experimental condition (H4, +Ac, -ATP, +Ac-ATP, for nucleus periphery and center),  $\tau_{\text{D}}$  and  $\tau_{\text{DA}}$  were obtained from Gaussian fits of  $\tilde{\tau}$  distributions in the absence and in the presence of dBD, respectively.

**Refractive index determination.** The refractive index  $n$  is related to the fluorescence lifetime  $\tau$  by the equation (29):

$$\tau^{-1} = 2.88 \times 10^{-9} \frac{n^2}{\Phi} \frac{\int I(v)dv}{\int I(v)v^{-3}dv} \int \frac{\varepsilon(v)}{v} dv,$$

in which  $\Phi$  is the quantum yield,  $I$  is the fluorescence emission intensity at the wave number  $v$  and  $\varepsilon$  is the extinction coefficient. The refractive index  $n$  was obtained from the calibration curve published elsewhere (30).

### High resolution and S/N intensity acquisition and analysis

Cells transfected or not with EGFP-H4 were stained with Hoechst 33342 (10  $\mu\text{M}$ , 30 min at 37°C) and imaged on a spinning disk CSU-W1 (Yokogawa, Andor) microscope (DMI8 Leica, Germany) equipped with lasers at 405 nm (100 mW) and 488 nm (150 mW) operating at 10% power and sCMOS camera (Orca-Flash V2<sup>+</sup>, Hamamatsu). Z stacks of EGFP-H4 (emission filter: 500–550 nm) and Hoechst (emission filter: 425–475 nm) images were acquired (300 ms per slice) through a 63 $\times$  NA = 1.4 oil objective. Pixel-by-pixel analysis on the equatorial plane was performed with MATLAB routines on nuclei segmented as above (Supplementary Figure S1C). To assess for possible biases, this segmentation approach was compared to line-scan analyses across intensity images of nuclei, where peripheral pixels were defined as those between the last border pixel from both line ends below about the background intensity plus its standard deviation and the next local minimum of intensity, and central pixels elsewhere in between.

### FCS measurements

FCS measurements were carried out on a confocal time-resolved microscope MicroTime 200 (Picoquant, Berlin, Germany) as described elsewhere (31). dBD-EGFP was excited at 470 nm by a pulsed diode laser (Picoquant) through an Olympus UPLSAPO water objective (60X/NA 1.2), for a 0.4 fL excitation volume. Fluorescence emission passes through a dichroic mirror (DM 470 nm, Picoquant) and is focused on a pinhole in front of an avalanche photodiode (SPADs 14, Perkin Elmer) through the emission filter FF01-525/50 (Picoquant). The TimeHarp 300 PC board (PicoQuant) acquires during 60 s single photon-counting time traces analyzed with the Symphotime software (PicoQuant). A two-species Brownian diffusion model was used to fit the fluorescence fluctuation auto-correlation function and retrieve amplitudes and apparent diffusion coefficients.

### FRAP experiments

FRAP (fluorescence recovery after photobleaching) experiments were carried out on a Zeiss AxioObserver Z.1 mi-

croscope equipped with a Yokogawa CSU22 spinning-disk head, a Zeiss Plan APO 63 $\times$ /1.4 NA oil objective and a CMOS camera (Photometrics PRIM95B back side illuminated, 11  $\mu\text{m}$  pixel size). A FRAP Head (Roper scientific) equipped with a 473 nm diode laser (50 mW) was used at 50% laser power with two repetitions of 22 ms each to perform 16 pixels region bleaching (diameter: 2.3  $\mu\text{m}$ , laser power before objective: 4.6 mW). Pre-bleach and post-bleach image acquisitions (200 ms acquisition time and time interval) were performed with a 491 nm diode laser. In these conditions, all fluorescent molecules in the bleached volume were photobleached and no fluorescence photobleaching occurred through imaging.

### Statistical analysis

Comparisons between treatments were performed with (unpaired, two-tailed) Kruskal–Wallis tests. Comparisons between Gaussian fits of peripheral and central distributions of fluorescence lifetimes and their fluctuations, and between linear fits of peripheral versus central intensities, were performed with extra sum-of-squares  $F$  tests and the null hypothesis that both data sets are better fitted together by a single curve rather than one each. Correlations were tested with extra sum-of-squares  $F$  tests and the null hypothesis that slopes of linear fits were 0. Difference of the slope from 1 was tested similarly. All of the above was performed in Prism V (GraphPad).

## RESULTS

### EGFP-H4 fluorescence lifetime reports chromatin condensation and its global and local heterogeneities

We imaged EGFP-H4 in live HEK cells. About 80% of EGFP-H4 was immobile as assessed by FRAP (fluorescence recovery after photobleaching) (Supplementary Figure S2A), supporting it was mainly incorporated in chromatin. We further verified that EGFP-H4 intensity spatially correlated with that of Hoechst in co-stained cells (Supplementary Figure S2B, C). Moreover, both intensities exhibited a radial differential (Supplementary Figure S2C, see Materials and Methods), independently on EGFP-H4 expression (Supplementary Figure S2D, E). Altogether, these results support that EGFP-H4 intensity reports endogenous concentrations of chromatin without visible artefact.

The nucleus was previously shown to exhibit a distinctive refractive index  $n \sim 1.39$  (32). The fluorescence lifetime of a fluorophore is sensitive to  $n$  (29,30), and was previously used with tagged proteins to probe it in live cells (33,34). Consistently, the time-averaged fluorescence lifetime  $\tilde{\tau}$  of EGFP-H4 yielded  $n \sim 1.40$  (see Materials and Methods). Moreover,  $\tilde{\tau}$  was slightly but significantly lower for EGFP-H4 than for EGFP alone, showing that tagged EGFP was sensitive to the presence of histones (Figure 1A, B). To validate that  $\tilde{\tau}$  reports chromatin condensation, we exposed cells to the histone de-acetylase inhibitor sodium butyrate for histone hyper-acetylation (+Ac) (Supplementary Figure S1A), or sodium azide and deoxy-glucose for ATP depletion (-ATP), which induce chromatin decondensation or condensation, respectively (5,18). In +Ac condition,  $\tilde{\tau}$  of EGFP-H4 appeared mildly but significantly higher than in untreated

condition. In  $-ATP$  condition,  $\tilde{\tau}$  was substantially and significantly lower than in untreated condition (Figure 1B). These results validate that  $\tilde{\tau}$  of EGFP-H4 decreases with chromatin condensation, similarly to Hoechst fluorescence lifetime (18). Additionally, ATP depletion reversed the effect of hyper-acetylation: the  $+Ac-ATP$  condition exhibited a  $\tilde{\tau}$  even lower than the  $-ATP$  condition only (Figure 1B). This reveals a functional interaction between histone acetylation state and ATP-dependent mechanisms.

Since  $\tilde{\tau}$  was broadly distributed in most conditions, we next examined whether these distributions contained spatially distinct sub-populations of condensed chromatin. Both peripheral and central nuclear regions exhibited normal distributions of  $\tilde{\tau}$  across pixels that were indistinguishable from each other for free EGFP (Figure 1C). In contrast,  $\tilde{\tau}$  of EGFP-H4 was on average significantly higher at the nuclear periphery than in the center ( $\Delta\tilde{\tau} \sim 0.02$  ns). Note that  $\tilde{\tau}$  was not normalized between cells, which implies that  $\tilde{\tau}$  intercellular variability is negligible in comparison to intranuclear variability. In  $+Ac$  conditions,  $\tilde{\tau}$  was also higher at the periphery than in the center ( $\Delta\tilde{\tau} > 0.01$  ns). In ATP-depleted cells in contrast, differences in  $\tilde{\tau}$  between peripheral and central regions were abolished for hyper-acetylated chromatin ( $+Ac-ATP$ ), or even reversed,  $\tilde{\tau}$  higher in the center than at the periphery ( $\Delta\tilde{\tau} \sim -0.007$  ns) in the absence of hyper-acetylation ( $-ATP$ ). Altogether, these results show that chromatin is actively less condensed at the nuclear periphery. In contrast, the chromatin concentration differential between peripheral and central regions, given by fluorescence intensity, was independent of acetylation or ATP (Supplementary Figure S2F). This indicates that chromatin higher-order structures vary without substantial concentration change and also supports no substantial contribution to  $\tilde{\tau}$  of possible changes in EGFP-H4 bound fraction across conditions. To ascertain this, we measured by FRAP the mobile fractions of EGFP-H4 in  $+Ac$ ,  $-ATP$  and  $+Ac-ATP$ , which magnitudes did not correlate with that of  $\tilde{\tau}$  (Supplementary Figure S2A).

To further characterize chromatin condensation spatial heterogeneities independently of the radial localization, we measured the spatial autocorrelation of the instantaneous lifetime  $\tau$  (see Materials and Methods). For EGFP-H4,  $\tau$  exhibited an autocorrelation length  $l$  of 600 nm, significantly higher than that of GFP alone (500 nm, the spatial resolution limit) (Supplementary Figure S2G), supporting the existence of  $\sim 600$  nm-radius domains of similar condensation state. Hyper-acetylation slightly but significantly increased the size of these domains compared to that in untreated cells. In contrast, ATP depletion had no significant effect, unless in hyper-acetylated condition, where it significantly decreased the size of same-condensation domains below the resolution limit. The opposite effects of hyper-acetylation as a function of ATP levels on  $l$ , consistent with that on  $\tilde{\tau}$ , further supports that histone state and cell metabolism interact to control condensation domain size: hyper-acetylation favors large domains of similar condensation in an ATP-dependent fashion, while it hinders the size of such domains in the absence of ATP.

## Fluctuations of chromatin condensation depend on sub-nuclear localization, histone acetylation and metabolic state

Since chromatin condensation exhibited spatial heterogeneities, we next examined whether and how it fluctuated in time. To quantify this, we measured the standard deviation of EGFP-H4 fluorescence lifetime temporal fluctuations,  $\sigma_\tau$  (see Materials and Methods). In untreated condition,  $\sigma_\tau$  of EGFP-H4 was significantly higher than that of GFP alone, supporting that these fluctuations were specific to the environment of histones (Figure 1D and E). Remarkably, ATP depletion increased  $\sigma_\tau$  compared to untreated cells, which indicates the existence of constitutive fluctuations that do not require ATP consumption. Moreover, these spontaneous fluctuations are hindered by ATP-dependent mechanisms. Hyper-acetylation in ATP-depleted condition ( $+Ac-ATP$ ) decreased  $\sigma_\tau$  compared to ATP-depletion alone ( $-ATP$ ), showing that ATP-independent, hyper-acetylation-dependent mechanisms also hinder spontaneous fluctuations. However, addition of both ATP and hyper-acetylation ( $+Ac$  condition) had on spontaneous fluctuations ( $-ATP$  condition) the mildest decrease compared to addition of any of the two (H4 untreated or  $+Ac-ATP$ ). This supports the existence of ATP- and hyper-acetylation-dependent mechanisms that out-compete the effects on spontaneous condensation fluctuations of mechanisms that only depend on ATP or hyper-acetylation.

We next examined the spatial organization of chromatin condensation fluctuations. For EGFP alone,  $\sigma_\tau$  was slightly higher at the periphery than in the center of the nucleus ( $\Delta\sigma_\tau < 0.005$  ns), showing that fluorescence lifetime fluctuations were somewhat sensitive to nuclear localization regardless of protein tagging. Nevertheless,  $\sigma_\tau$  of EGFP-H4 in all conditions exhibited between nuclear periphery and center a significant difference that was at least twice larger than that of EGFP alone ( $\Delta\sigma_\tau > 0.01$  ns) (Figure 1F), consistent with chromatin condensation fluctuation amplitudes at the periphery larger than in the center of the nucleus, in all conditions. Thus, chromatin condensation and its fluctuations both exhibit radial organizations within the nucleus. Nevertheless, the radial organizations of condensation and its fluctuations are distinctly regulated since they respond differently upon acetylation and metabolic perturbations.

## Cell metabolism is required for chromatin de-condensation to correlate with its fluctuations

To clarify the relation between chromatin condensation and its fluctuations, we directly assessed their level of correlation in a pixel-by-pixel, non-spatially biased approach (Figure 2A). While EGFP did not exhibit a correlation between  $\tilde{\tau}$  and  $\sigma_\tau$  ( $r = -0.1759$ ), EGFP-H4 did in untreated condition ( $r = 0.5318$ ) as well as in  $+Ac$  condition ( $r = 0.4829$ ). Compared to untreated cells, ATP depletion alone led to weak anti-correlation ( $r = -0.2447$ ), and within a hyper-acetylated background to a loss of correlation ( $r = 0.0942$ ). Thus, correlation between  $\tilde{\tau}$  and  $\sigma_\tau$  is largely acetylation-independent but strongly ATP-

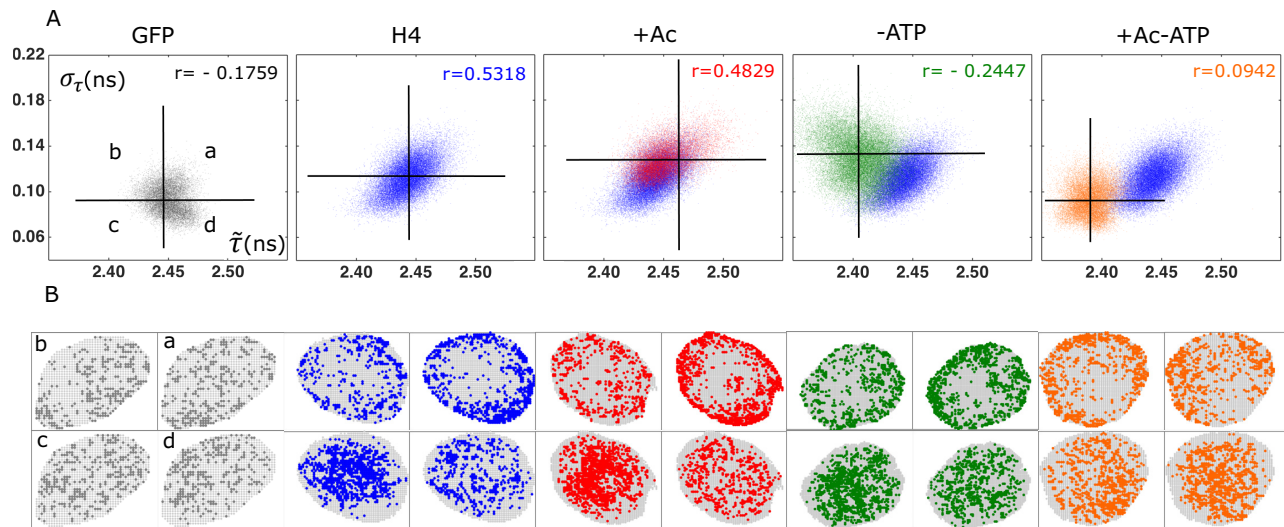


**Figure 2.** Correlation of chromatin de-condensation with chromatin condensation fluctuations depends on metabolic state. (A)  $\sigma_\tau - \tilde{\tau}$  plots for free EGFP or EGFP-H4 in untreated (H4), hyper-acetylation (+Ac), ATP-depletion (−ATP), or both (+Ac-ATP) conditions and their respective correlation coefficients. Same pixel and cell numbers as in Figure 1. Values for untreated cells are displayed in blue along all other conditions for visual comparison. Horizontal and vertical lines cross at  $\sigma_\tau$  and  $\tilde{\tau}$  means. (B) Typical localization in a nucleus of pixels from the four quadrants defined above.

dependent. Correlation reversal upon ATP depletion further confirms that ATP-dependent mechanisms promoting chromatin de-condensation simultaneously hinder spontaneous chromatin fluctuations.

To assess how this correlation was related to chromatin localization, we split the pixel population in four quadrants around the mean  $\tilde{\tau}$  and  $\sigma_\tau$  and mapped them on the nucleus (Figure 2B). For EGFP alone, pixels of all quadrants distributed throughout the nucleus in both peripheral and central regions. For EGFP-H4 in contrast, pixels from high  $\sigma_\tau$  quadrants (a, b) were largely excluded from the central region, and pixels from the low  $\tilde{\tau}$  and  $\sigma_\tau$  quadrant (c) were more abundant at the center than that of any other quadrant. Compared to untreated cells, hyper-acetylation or ATP depletion did not substantially change this pattern, thus confirming previous results (Figure 1) that central/peripheral heterogeneities in chromatin fluctuations are robust to metabolic changes and acetylation of histones.

#### H4 histones interact with dBD except in cells both hyper-acetylated and ATP-depleted

To better understand the effect of chromatin condensation and its fluctuations on accessibility of protein factors, we first sought to assess the interaction of the TAF<sub>11250</sub>-double bromodomain (dBD) with acetylated H4 histones by FCS (Fluorescence fluctuation correlation spectroscopy). In cells exogenously expressing dBD-GFP, FCS showed the protein sorted in two populations: ~12% of dBD-GFP exhibited an apparent diffusion coefficient of  $0.3 \mu\text{m}^2 \text{s}^{-1}$ , consistent with that of a population interacting with an immobile ligand, the rest exhibited an apparent coefficient of about  $4 \mu\text{m}^2 \text{s}^{-1}$ , consistent with a protein diffusing much more freely (Table S1). In hyper-acetylation conditions, the slow population exhibited an apparent diffusion coefficient indistinguishable from that of the slow population in un-

treated conditions and its fraction increased to ~20% of total dBD-GFP. Thus, an interaction specific to acetylated H4 histones occurs with dBD-GFP, as expected (35).

We thus proceeded to directly assess the interaction between EGFP-H4 and dBD-mCherry. Compared to cells expressing EGFP-H4 alone, cells expressing both EGFP-H4 and dBD-mCherry exhibited a nuclear map of EGFP-H4  $\tilde{\tau}$  shifted to lower values (Figure 3A, B). Significantly, both peripheral and central regions of the nucleus exhibited lower  $\tilde{\tau}$  in the presence of dBD-mCherry than in its absence ( $\Delta\tilde{\tau} > 0.04$  ns and 0.02 ns, respectively), indicating that FRET, and thereby an interaction occurs between EGFP-H4 and dBD-mCherry, and apparently to a larger extent at the periphery (Figure 3C). In contrast,  $\tilde{\tau}$  of EGFP-H4 in cells expressing mCherry alone exhibited only a modest shift ( $\Delta\tilde{\tau} < 0.02$  ns) that cannot account for the drop due to the dBD (Supplementary Figure S3A). Thus, the interaction is specific to the dBD. In hyper-acetylation conditions, both peripheral and central regions of the nucleus exhibited lower  $\tilde{\tau}$  in the presence of dBD-mCherry and to a larger extent than without hyper-acetylation ( $\Delta\tilde{\tau} > 0.06$  ns and 0.04 ns, respectively), consistently with the interaction specificity to acetylated histones. The accessibility increase upon hyper-acetylation is, however, somewhat modest when compared to the extent of hyper-acetylation (Supplementary Figure S1A), in support of acetylation being a poor predictor of accessibility. In ATP depleted cells,  $\tilde{\tau}$  also exhibited a drop in the presence of dBD-mCherry both at the periphery and the center ( $\Delta\tilde{\tau} > 0.05$  ns and 0.03 ns, respectively). This shows that accessibility of dBD to H4 histones does not require ATP, just as chromatin fluctuations do, and still occurs in condensed chromatin conditions (see Figure 1). However, in hyper-acetylated and ATP-depleted cells, the drop in  $\tilde{\tau}$  was dramatically reduced of near an order of magnitude both at the periphery and the center ( $\Delta\tilde{\tau} < 0.01$  ns and 0.001 ns, respectively) such that  $\tilde{\tau}$  distributions at the center with or without dBD were indistinguishable, in



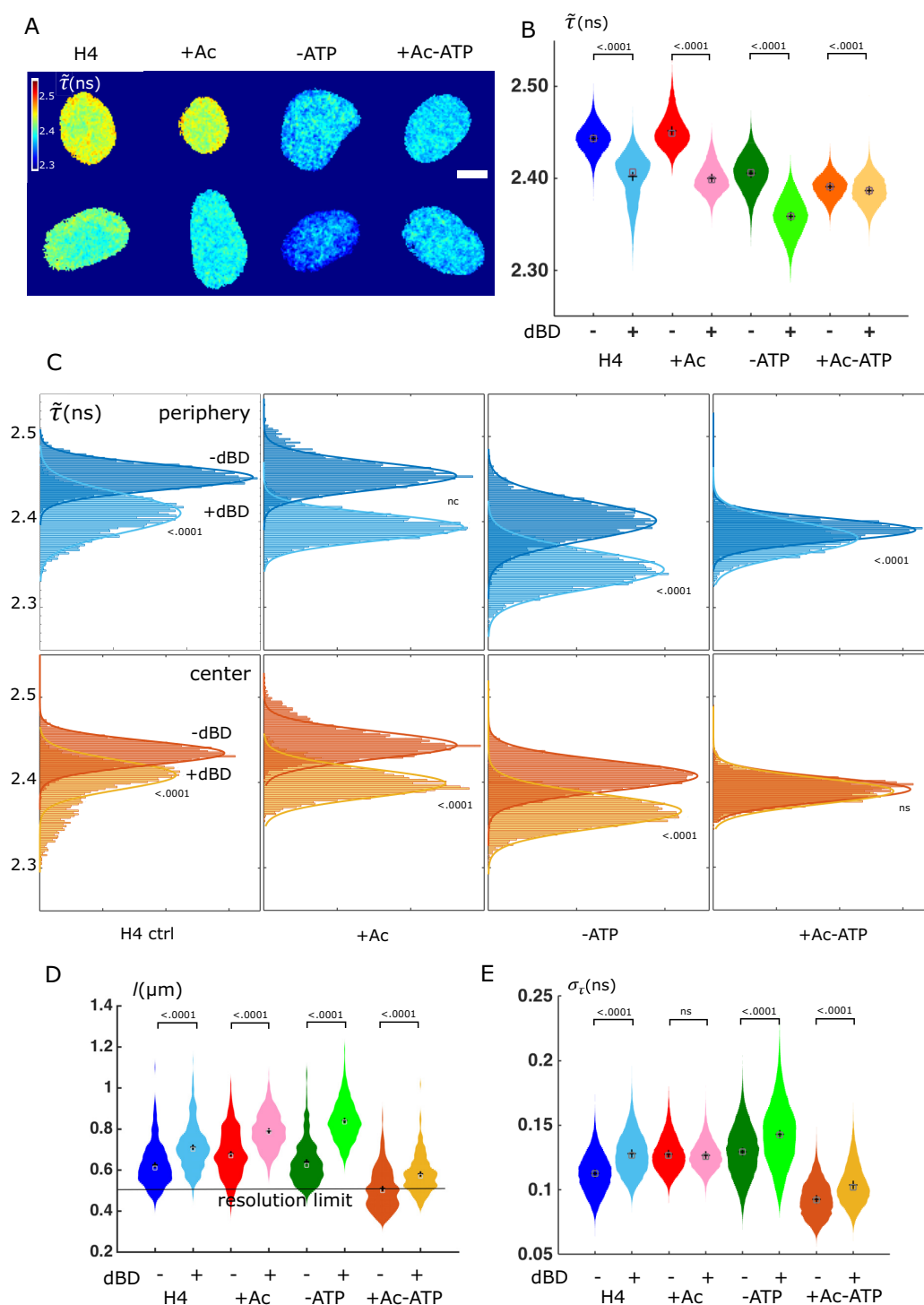


**Figure 3.** Chromatin accessibility and its fluctuations depend on subnuclear localization, histone acetylation and metabolic state (A) Typical images of time-averaged fluorescence lifetime  $\tilde{\tau}$  in HEK cells expressing EGFP-H4 in untreated (H4), hyper-acetylation (+Ac), ATP-depletion (-ATP), or both (+Ac-ATP) conditions, in the absence (top) or presence (bottom) of dBD-mCherry. Bar = 5  $\mu\text{m}$ . (B) Time-averaged fluorescence lifetime  $\tilde{\tau}$  distributions in conditions above. Same data as in Figure 1 for absent dBD-mCherry, otherwise EGFP-H4 (16 474 pixels, eight cells); +Ac (19 146 pixels, nine cells); -ATP (24 432 pixels, 13 cells); +Ac-ATP (21 026 pixels, eight cells). Black cross: mean, grey box: median. Kruskal-Wallis test. (C) Time-averaged fluorescence lifetime  $\tilde{\tau}$  distributions in conditions above for peripheral and central pixels and their Gaussian fits. Same as in Figure 1 for absent dBD-mCherry. Extra sum-of-squares F test with same fit for both distributions as null hypothesis. ns = not significant, nc = not convergent (for a same fit for both distributions). (D) Correlation length/distributions in conditions above. Same data as in Supplementary Figure S2G for absent dBD-mCherry, otherwise EGFP-H4 (16 474 pixels, eight cells); +Ac (19 146 pixels, nine cells); -ATP (24 432 pixels, 13 cells); +Ac-ATP (21 026 pixels, eight cells). Black cross: mean, grey box: median. Kruskal-Wallis test. (E) Distributions of fluorescence lifetime standard deviation  $\sigma_r$  in conditions above. Same data as in Figure 1 for absent dBD-mCherry, otherwise EGFP-H4 (16 474 pixels, eight cells); +Ac (19 146 pixels, nine cells); -ATP (24 432 pixels, 13 cells); +Ac-ATP (21 026 pixels, eight cells). Black cross: mean, grey box: median. Kruskal-Wallis test. ns = not significant.

the only condition that also led to a substantial decrease in chromatin fluctuations (see above). Therefore, acetylation does not predict accessibility in this case. Finally, the drops in  $\tilde{\tau}$  were in all conditions larger at the periphery than in the center of the nucleus, just as fluctuations were (Figure 1).

### Chromatin accessibility domains are larger than condensation domains and accessibility fluctuations are restricted by hyper-acetylation in an ATP-dependent fashion

In the presence of dBD, similarly to  $\Delta\tilde{\tau}$  reporting chromatin accessibility,  $l$  and  $\Delta\sigma_\tau$  may report the typical size of same-accessibility domains and the occurrence of temporal fluctuations of accessibility, respectively.

In the presence of dBD,  $l$  was higher than in its absence in all conditions examined ( $\Delta l > 72$  nm), which indicates that same-accessibility chromatin domains are larger than same-condensation domains (Figure 3D). The spontaneous fluctuation condition (–ATP) exhibited the largest same-accessibility domains ( $l = 840$  nm) and the decrease in same-accessibility domain size was smaller upon addition of ATP and hyper-acetylation together ( $\Delta l = 50$  nm) than upon any of the two ( $\Delta l = 128$  nm and  $\Delta l = 260$  nm, respectively). Moreover, the discrepancy between condensation and accessibility domains sizes also decreased less upon addition of ATP and hyper-acetylation ( $\Delta l = 72$  nm) than upon any of the two ( $\Delta l = 86$  nm and  $\Delta l = 112$  nm, respectively). Altogether, this indicates the existence of hyper-acetylation and ATP-dependent mechanisms partly independent of chromatin condensation domains size that individually restrict same-accessibility chromatin domains size but are out-competed by ATP- and hyper-acetylation-dependent mechanisms.

In the presence of dBD,  $\sigma_\tau$  was substantially higher than in its absence in all but the hyper-acetylated condition ( $\Delta\sigma_\tau > 0.011$  ns) (Figure 3E). In contrast, mCherry alone did not significantly affect  $\sigma_\tau$  (Supplementary Figure S3B). This indicates that significant accessibility fluctuations occur in addition to condensation fluctuations. Nevertheless, the lack of significant difference in  $\sigma_\tau$  with and without dBD in hyper-acetylated cells (+Ac) reveals that in this condition, accessibility fluctuations are strictly regulated such that overall  $\sigma_\tau$  amplitudes do not exceed that of condensation fluctuations.

### Chromatin condensation fluctuations predict chromatin accessibility

So far, our results support that chromatin accessibility is granted provided sufficient chromatin fluctuations occur, regardless of chromatin steady-state condensation or acetylation. To characterize this more quantitatively, we sought to assess the correlation, throughout all experimental conditions, between  $\sigma_\tau$  or  $\tilde{\tau}$  on the one hand, and the extent of FRET on the other hand. We found that the mean FRET transfer rate  $k\text{FRET}$  (see Material and Methods) significantly correlated with  $\sigma_\tau$  ( $r^2 = 0.8783$ ,  $P < 0.001$ ) while it did not with  $\tilde{\tau}$  ( $r^2 = 0.421$ ,  $P > 0.08$ ) (Figure 4A). These results support that chromatin accessibility is sensitive to chromatin condensation fluctuations amplitudes rather than chromatin condensation level.

To substantiate this further, we assessed the correlation of same-accessibility domain size  $l_{\text{dBD}}$  with same-condensation domain size  $l$  and with condensation fluctuation amplitudes  $\sigma_\tau$  (Figure 4B). Consistently, we found that same-accessibility domain size significantly correlated with condensation fluctuation amplitudes ( $r^2 = 0.971$ ,  $P < 0.02$ ), whereas it did not with same-condensation domain size ( $r^2 = 0.8002$ ,  $P > 0.1$ ). Thus, accessibility is favored when accessible and inaccessible domains are better segregated, regardless of condensation domains mixing.

Altogether, these results show that chromatin accessibility is predicted by chromatin condensation fluctuations rather than steady-state.

## DISCUSSION

Accumulating data on chromatin reporters demonstrate that chromatin in the interphase nucleus undergoes various modes of fluctuations. Localization microscopy provides chromatin density fluctuations at the nm scale (36,37). Single particle tracking shows chromatin motions over submicron distances as fast as within the 10 ms timescale (18–20). At the opposite end, displacement correlation spectroscopy shows motions at the 1–10 s timescales over several microns (21). Here, the fluorescence lifetime fluctuations we measure are in an intermediate range (~seconds timescale and  $> 100$  nm length scale) that corresponds to domains of  $\sim 4 \times 10^4$  nucleosomes, assuming a nucleosome concentration of 100  $\mu\text{M}$  (38). Thus, chromatin exhibits condensation fluctuations with same-condensation domain sizes well above the nucleosome array scale.

We have evidenced three remarkable features of these chromatin condensation fluctuations. First, these fluctuations are spontaneous (Figure 1). In agreement, *in vitro* reconstitution studies have shown that both individual nucleosomes and nucleosome arrays undergo spontaneous conformational fluctuations across the  $\mu\text{sec}$  to min timescales (39–41), and fixed cells also exhibit nucleosome fluctuations (20). We propose that the activity of ATP-dependent chromatin remodelers is, to some extent, detrimental to spontaneous chromatin condensation fluctuations (Figure 4C), although we cannot exclude that other, more distant or indirect ATP-dependent processes may be involved, too. This is in stark contrast with the ATP-dependence of chromatin de-condensation (Figure 1). Thus, chromatin de-condensation and its fluctuations are supported by fundamentally distinct mechanisms. Second, chromatin fluctuations are intrinsically dependent on chromatin sub-nuclear localization that cannot be explained solely from heterogeneities in histone acetylation and ATP-dependent remodeling activity (Figure 1). Thus, sub-nuclear spatial cues constitute a distinct pathway regulating chromatin fluctuations. This is, again, in stark contrast with chromatin condensation, although which exhibits spatial heterogeneity, requires ATP to do so (Figure 1). Third, we identify (i) acetylation-independent, ATP-dependent mechanisms and (ii) acetylation-dependent, ATP-independent mechanisms that each decrease spontaneous fluctuations, but these are out-competed by (iii) acetylation- and ATP-dependent mechanisms restoring fluctuations closer to their spontaneous level (Figure 1). We propose that (i) ATP hinders



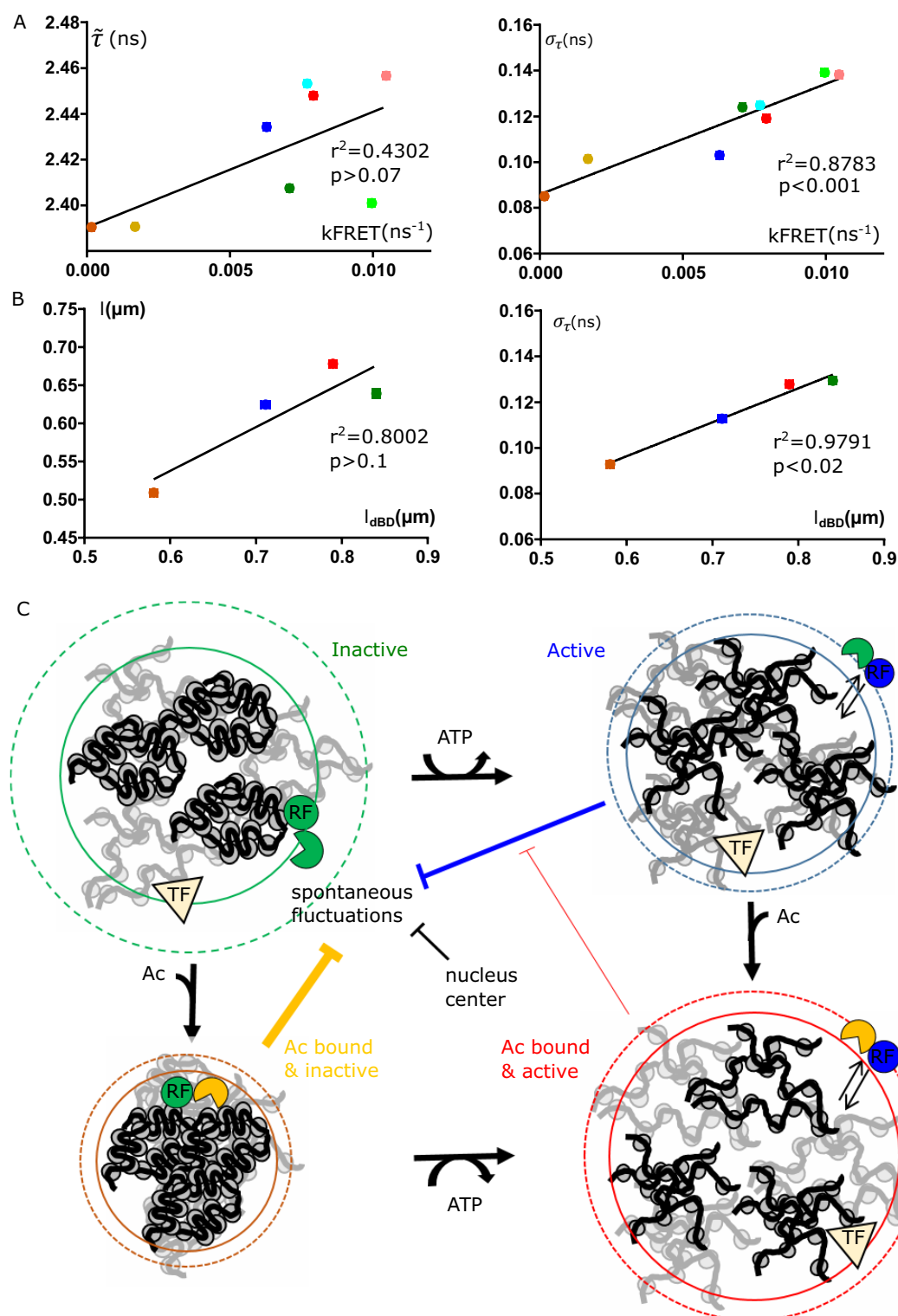


**Figure 4.** Chromatin condensation fluctuations, rather than steady-state, predict chromatin accessibility. (A) Time-averaged fluorescence lifetime  $\bar{\tau}$  (left) and standard deviation  $\sigma_{\tau}$  (right) as a function of  $kFRET$  in all conditions (blue: H4, red: +Ac, green: -ATP, brown: +Ac-ATP) and sub-nuclear regions (dark: center, pale: periphery). Data are mean  $\pm$  SEM of Gaussian fits from data shown in Figure 1C and F. Solid lines are linear fits, correlation coefficients displayed. Extra sum-of-squares  $F$  test with slope = 0 as null hypothesis. (B) Fluorescence lifetime spatial correlation length  $l$  (left) and standard deviation  $\sigma_{\tau}$  (right) as a function of spatial correlation in the presence of dBD  $l_{dBD}$  in all conditions (blue: H4, red: +Ac, green: -ATP, brown: +Ac-ATP). Data are mean  $\pm$  SEM of whole nucleus distributions from (Figures 1E and 3D). Solid lines are linear fits, correlation coefficients displayed. Extra sum-of-squares  $F$  test with slope = 0 as null hypothesis. (C) Mechanisms regulating spontaneous fluctuations of chromatin condensation. TF: transcription factor, RF: ATP-dependent and acetylation-binding remodeling factor and its state (active/inactive, Ac bound or not). Plain circle: same-condensation domain size, dashed circle: same accessibility domain size. See text for details.

spontaneous fluctuations through activation of acetylation-independent, transcriptional repressor-associated remodeling complexes, (ii) factors binding to acetylated chromatin restrict spontaneous chromatin condensation fluctuations in the absence of ATP, but that (iii) ATP promotes the release of these factors, thereby relieving part of the hindrance (Figure 4C). Indeed, ligands of acetylated chromatin are widespread among ATP-dependent remodeling complexes (27), and the release from chromatin of one of them was previously found to require ATP (42). Furthermore, in hyper-acetylated conditions, the presence of ATP may, in addition, facilitate acetylation propagation, and thereby fluctuations, on adjacent nucleosomes by acetyltransferases (43) consistent with the growth of same-condensation domains in these conditions (Supplementary Figure S2G). Mechanisms of interplay between chromatin acetylation and ATP-dependent remodeling are currently being revealed (44,45). Future studies will address the identification of the factors involved here.

Genome accessibility has mostly been assessed with biochemical approaches on isolated nuclei on the basis of DNA sensitivity to some enzymatic activity (digestion, methylation...) (46). These approaches are essentially sensitive to the presence of nucleosomes along the DNA double-strand and poorly account for the effects on accessibility of higher-order chromatin structures above the nucleosomal array scale. Besides, a number of fluorescence imaging modalities has been applied to assess intranuclear milieu permeability to inert fluorescent particles or chromatin interactants (14–17,20,47). These approaches have shown that, although histone modifications affect permeability at scales above that of nucleosomal arrays, chromatin can be almost as permeable regardless of its condensation state. Moreover, if effects on interactant binding to chromatin were assessed, they were done so only indirectly. Using FRET between chromatin and a domain of transcription factors, we show here that the level of nucleosomal-scale direct accessibility is similar across distances of orders of magnitude larger than the nucleosome size and is not restricted by condensation. Instead, condensed chromatin exists in distinct fluctuation states with distinct accessibilities, which may explain inconsistencies between previously reported condensed chromatin permeability (14,20). We show that chromatin accessibility to acetylated histones, as its condensation fluctuations, is spontaneous and not predicted from the acetylation level. We propose that a fraction of acetylated histones is made accessible by condensation fluctuations upon ATP-dependent release of acetylation- and ATP-dependent binding factors, while another fraction remains inaccessible due to acetylation-dependent histone–DNA interactions (8) or other binding factors that prevent condensation fluctuations. Whether this fraction organizes as in previously reported sub-diffraction domains remains to be determined (22,48). Other ATP- and hyper-acetylation-dependent mechanisms may also account for the limited accessibility of acetylated histones, as fluctuations of accessibility are restricted to a level indistinguishable from condensation fluctuations in the presence of both ATP and hyper-acetylation.

Finally, our results consistently show that, on average, peripheral chromatin is more accessible, less condensed, and

less concentrated than central chromatin. Although this is consistent with repeated observations of less concentrated and more accessible peripheral chromatin (12,47), this may appear at odds with prior reports of gene-poor chromatin at, and translocation upon activation of some genes from, the nuclear periphery. We have previously shown, however, that cell fixation and permeabilization, as required for electron microscopy, results in artefactual chromatin condensation at the nuclear periphery (23). It is also clear now that the relation between gene activity and radial positioning is more complex than previously thought (49). While further investigation will be required to reveal the extent of the functional relevance of chromatin accessibility as we measure it, we show here that the critical determinant for this chromatin accessibility is its condensation fluctuations, rather than its condensation steady-state. These fluctuations are spontaneous, intrinsically dependent on sub-nuclear localization, and under the control of distinct and competing mechanisms dependent on acetylation, ATP and both.

## SUPPLEMENTARY DATA

Supplementary Data are available at NAR Online.

## ACKNOWLEDGEMENTS

We thank Xavier Baudin and Vincent Contremoulins of ImagoSeine facility of the Institut Jacques Monod, member of France BioImaging infrastructure, for advice and assistance on image acquisition and analysis, Sophie Polo for critical reading of the manuscript, and Mathieu Coppey for custom-built MATLAB routines, discussions and critical reading of the manuscript.

## FUNDING

IBISA; Fondation Recherche Médicale; Centre National de la Recherche Scientifique; Institut National de la Santé et de la Recherche Médicale; France BioImaging infrastructure [ANR-10-INBS-04]. Funding for open access charge: Centre National de la Recherche Scientifique.

*Conflict of interest statement.* None declared.

## REFERENCES

- Allfrey, V.G., Faulkner, R. and Mirsky, A.E. (1964) Acetylation and methylation of histones and their possible role in the regulation of RNA synthesis. *Proc. Natl Acad. Sci. U.S.A.*, **51**, 786–794.
- Hong, L., Schroth, G.P., Matthews, H.R., Yau, P. and Bradbury, E.M. (1993) Studies of the DNA binding properties of histone H4 amino terminus. Thermal denaturation studies reveal that acetylation markedly reduces the binding constant of the H4 “tail” to DNA. *J. Biol. Chem.*, **268**, 305–314.
- Norton, V.G., Imai, B.S., Yau, P. and Bradbury, E.M. (1989) Histone acetylation reduces nucleosome core particle linking number change. *Cell*, **57**, 449–457.
- Lee, D.Y., Hayes, J.J., Pruss, D. and Wolffe, A.P. (1993) A positive role for histone acetylation in transcription factor access to nucleosomal DNA. *Cell*, **72**, 73–84.
- Lières, D., James, J., Swift, S., Norman, D.G. and Lamond, A.I. (2009) Quantitative analysis of chromatin compaction in living cells using FLIM-FRET. *J. Cell Biol.*, **187**, 481–496.
- Shogren-Knaak, M., Ishii, H., Sun, J.M., Pazin, M.J., Davie, J.R. and Peterson, C.L. (2006) Histone H4-K16 acetylation controls chromatin structure and protein interactions. *Science*, **311**, 844–847.

7. Sasaki, K., Ito, T., Nishino, N., Khochbin, S. and Yoshida, M. (2009) Real-time imaging of histone H4 hyperacetylation in living cells. *Proc. Natl Acad. Sci. U.S.A.*, **106**, 16257–16262.
8. Potoyan, D.A. and Papoian, G.A. (2012) Regulation of the H4 tail binding and folding landscapes via Lys-16 acetylation. *Proc. Natl Acad. Sci. U.S.A.*, **109**, 17857–17862.
9. Weintraub, H. (1985) High-resolution mapping of S1- and DNase I-hypersensitive sites in chromatin. *Mol. Cell Biol.*, **5**, 1538–1539.
10. Tsompana, M. and Buck, M.J. (2014) Chromatin accessibility: a window into the genome. *Epigenet. Chromatin*, **7**, 33–49.
11. Klemm, S.L., Shipony, Z. and Greenleaf, W.J. (2019) Chromatin accessibility and the regulatory epigenome. *Nat. Rev. Genet.*, **20**, 207–220.
12. Chen, X., Shen, Y., Draper, W., Buenrostro, J.D., Litzenburger, U., Cho, S.W., Satpathy, A.T., Carter, A.C., Ghosh, R.P., East-Seletsky, A. et al. (2016) ATAC-se reveals the accessible genome by transposase-mediated imaging and sequencing. *Nat. Methods*, **13**, 1013–1020.
13. Phair, R.D. and Misteli, T. (2000) High mobility of proteins in the mammalian cell nucleus. *Nature*, **404**, 604–609.
14. Görisch, S.M., Wachsmuth, M., Tóth, K.F., Lichter, P. and Rippe, K. (2005) Histone acetylation increases chromatin accessibility. *J. Cell Sci.*, **118**, 5825–5834.
15. Schmiedeberg, L., Weisshart, K., Diekmann, S., Meyer Zu Hoerste, G. and Hemmerich, P. (2004) High- and low-mobility populations of HP1 in heterochromatin of mammalian cells. *Mol. Biol. Cell*, **15**, 2819–2833.
16. Hinde, E., Cardarelli, F. and Gratton, E. (2015) Spatiotemporal regulation of Heterochromatin Protein 1- alpha oligomerization and dynamics in live cells. *Sci. Rep.*, **5**, 12001–12011.
17. Hinde, E., Cardarelli, F., Digan, M.A. and Gratton, E. (2010) In vivo pair correlation analysis of EGFP intranuclear diffusion reveals DNA-dependent molecular flow. *Proc. Natl. Acad. Sci. U.S.A.*, **107**, 16560–16565.
18. Spagnol, S.T. and Noel Dahl, K. (2014) Active cytoskeletal force and chromatin condensation independently modulate intranuclear network fluctuations. *Integr. Biol.*, **6**, 523–531.
19. Levi, V., Ruan, Q., Plutz, M., Belmont, A.S. and Gratton, E. (2005) Chromatin dynamics in interphase cells revealed by tracking in a Two-Photon excitation microscope. *Biophys. J.*, **89**, 4275–4285.
20. Hihara, S., Pack, C.G., Kaizu, K., Tani, T., Hanafusa, T., Nozaki, T., Takemoto, S., Yoshimi, T., Yokota, H., Imamoto, N. et al. (2012) Local nucleosome dynamics facilitate chromatin accessibility in living mammalian cells. *Cell Rep.*, **2**, 1645–1656.
21. Zidovska, A., Weitz, D.A. and Mitchison, T.J. (2013) Micron-scale coherence in interphase chromatin dynamics. *Proc. Natl Acad. Sci. U.S.A.*, **110**, 15555–15560.
22. Nozaki, T., Imai, R., Tanbo, M., Nagashima, R., Tamura, S., Tani, T., Joti, Y., Tomita, M., Hibino, K., Kanemaki, M.T. et al. (2017) Dynamic organization of chromatin domains revealed by super-resolution live-cell imaging. *Mol. Cell*, **67**, 282–293.
23. Tramier, M., Kemnitz, K., Durieux, C., Coppey, J., Denjean, P., Pansu, R.B., Coppey-Moisán, M. et al. (2000) Restrained torsional dynamics of nuclear DNA in living proliferative mammalian cells. *Biophys. J.*, **78**, 2614–2627.
24. Kanno, T., Kanno, Y., Siegel, R.M., Jang, M.K., Lenardo, M.J. and Ozato, K. (2004) Selective recognition of acetylated histones by bromodomain proteins visualized in living cells. *Mol. Cell*, **13**, 33–43.
25. Padilla-Parra, S., Audugé, N., Coppey-Moisán, M. and Tramier, M. (2008) Quantitative FRET analysis by fast acquisition time domain FLIM at high spatial resolution in living cells. *Biophys. J.*, **95**, 2976–2988.
26. Jeanmougin, F., Wurtz, J.-M., Le Douarin, B., Chambon, P. and Losson, R. (1997) The bromodomain revisited. *Trends Biochem. Sci.*, **22**, 151–153.
27. Filippakopoulos, P., Picaud, S., Mangos, M., Keates, T., Lambert, J.-P., Barsyte-Lovejoy, D., Felletar, I., Volkmer, R., Müller, S., Pawson, T. et al. (2012) Histone recognition and Large-Scale structural analysis of the human bromodomain family. *Cell*, **149**, 214–231.
28. Förster, T. (1948) Zwischenmolekulare Energiewanderung und Fluoreszenz. *Ann. Phys.*, **437**, 55–75.
29. Strickler, S.J. and Berg, R.A. (1962) Relationship between absorption intensity and fluorescence lifetime of molecules. *J. Chem. Phys.*, **37**, 814–822.
30. Suhling, K., Siegel, J., Phillips, D., French, P.M., Lévêque-Fort, S., Webb, S.E. and Davis, D.M. (2002) Imaging the environment of green fluorescent protein. *Biophys. J.*, **83**, 3589–3595.
31. Padilla-Parra, S., Audugé, N., Coppey-Moisán, M. and Tramier, M. (2011) Dual-color fluorescence lifetime correlation spectroscopy to quantify protein-protein interactions in live cell. *Microsc. Res. Tech.*, **74**, 788–793.
32. Brunsting, A. and Mullaney, P.F. (1974) Differential light scattering from spherical mammalian cells. *Biophys. J.*, **14**, 439–453.
33. van Manen, H.-J., Verkuijlen, P., Wittendorp, P., Subramaniam, V., van den Berg, T.K., Roos, D. and Otto, C. (2008) Refractive index sensing of green fluorescent proteins in living cells using fluorescence lifetime imaging microscopy. *Biophys. J.*, **94**, L67–L69.
34. Treanor, B., Lanigan, P.M., Suhling, K., Schreiber, T., Munro, I., Neil, M.A., Phillips, D., Davis, D.M. and French, P.M. (2005) Imaging fluorescence lifetime heterogeneity applied to GFP-tagged MHC protein at an immunological synapse. *J. Microsc.*, **217**, 36–43.
35. Jacobson, R.H., Ladurner, A.G., King, D.S. and Tjian, R. (2000) Structure and function of a human TAFII250 double bromodomain module. *Science*, **288**, 1422–1425.
36. Bohn, M., Diesinger, P., Kaufmann, R., Weiland, Y., Müller, P., Gunkel, M., von Ketteler, A., Lemmer, P., Hausmann, M., Heermann, D.W. et al. (2010) Localization microscopy reveals expression-dependent parameters of chromatin nanostructure. *Biophys. J.*, **99**, 1358–1367.
37. Ricci, M.A., Manzo, C., García-Parajo, M.F., Lakadamyali, M. and Cosma, M.P. (2015) Chromatin fibers are formed by heterogeneous groups of nucleosomes in vivo. *Cell*, **160**, 1145–1158.
38. Weidemann, T., Wachsmuth, M., Knoch, T.A., Müller, G., Waldeck, W. and Langowski, J. (2003) Counting nucleosomes in living cells with a combination of fluorescence correlation spectroscopy and confocal imaging. *J. Mol. Biol.*, **334**, 229–240.
39. Li, G., Levitus, M., Bustamante, C. and Widom, J. (2005) Rapid spontaneous accessibility of nucleosomal DNA. *Nat. Struct. Mol. Biol.*, **12**, 46–53.
40. Ngo, T.T.M. and Ha, T. (2015) Nucleosomes undergo slow spontaneous gaping. *Nucleic Acids Res.*, **43**, 3964–3971.
41. Poirier, M.G., Oh, E., Tims, H.S. and Widom, J. (2009) Dynamics and function of compact nucleosome arrays. *Nat. Struct. Mol. Biol.*, **16**, 938–944.
42. Lungu, C., Muegge, K., Jeltsch, A. and Jurkowska, R.Z. (2015) An ATPase-Deficient variant of the SNF2 family member HELLS shows altered dynamics at Pericentromeric heterochromatin. *J. Mol. Biol.*, **427**, 1903–1915.
43. Margueron, R. and Reinberg, D. (2010) Chromatin structure and the inheritance of epigenetic information. *Nat. Rev. Genet.*, **11**, 285–296.
44. Doiguchi, M., Nakagawa, T., Imamura, Y., Yoneda, M., Higashi, M., Kubota, K., Yamashita, S., Asahara, H., Iida, M., Fujii, S. et al. (2016) SMARCA1 is an ATP-dependent stimulator of nucleosomal H2A acetylation via CBP, resulting in transcriptional regulation. *Sci. Rep.*, **6**, 20179–20191.
45. Denslow, S.A. and Wade, P.A. (2007) The human Mi-2/NuRD complex and gene regulation. *Oncogene*, **26**, 5433–5438.
46. Bell, O., Tiwari, V.K., Thomä, N.H. and Schübeler, D. (2011) Determinants and dynamics of genome accessibility. *Nat. Rev. Genet.*, **12**, 554–564.
47. Bancaud, A., Huet, S., Daigle, N., Mozziconacci, J., Beaudouin, J. and Ellenberg, J. (2009) Molecular crowding affects diffusion and binding of nuclear proteins in heterochromatin and reveals the fractal organization of chromatin. *EMBO J.*, **28**, 3785–3798.
48. Boettiger, A.N., Bintu, B., Moffitt, J.R., Wang, S., Believeau, B.J., Fudenberg, G., Imakaev, M., Mirny, L.A., Wu, C.-T. and Zhuang, X. (2016) Super-resolution imaging reveals distinct chromatin folding for different epigenetic states. *Nature*, **529**, 418–422.
49. Takizawa, T., Meaburn, K.J. and Misteli, T. (2008) The meaning of gene positioning. *Cell*, **135**, 9–13.